The Astrophysical Journal, 601:885–895, 2004 February 1

EFFECTS OF THERMAL CONDUCTION ON THE X-RAY AND SYNCHROTRON EMISSION FROM SUPERNOVA REMNANTS

Pablo F. Velázquez, Julio J. Martinell, and Alejandro C. Raga
Instituto de Ciencias Nucleares, Universidad Nacional Autónoma de México, Apartado Postal 70-543, CP 04510, México DF, Mexico;
pablo@nuclecu.unam.mx, jjmb@nuclecu.unam.mx, raga@nuclecu.unam.mx

and

Elsa B. Giacani
Instituto de Astronomía y Física del Espacio, Ciudad Universitaria, Pabellón IAFE, CC 67, CP 1428, Buenos Aires, Argentina; egiacani@iafe.uba.ar
Received 2003 June 12; accepted 2003 October 14

ABSTRACT

Several physical mechanisms have been studied in order to explain why composite supernova remnants (SNRs) have shell-like morphologies in the radio continuum while their X-ray emission is centrally peaked. One of the proposed mechanisms has been the presence of thermal conduction, which can raise the density at the center of SNRs, increasing the X-ray emission from these regions. In this work, we have carried out axisymmetric numerical simulations with the adaptive grid Yguazú-a code, which includes advection of the magnetic field and thermal conduction. We have considered cases with anisotropic and isotropic thermal conduction, as well as with no conduction. We have simulated X-ray (as well as radio synchrotron) emission maps from our numerical simulations, which can be directly compared with observations.

Subject headings: conduction — ISM: magnetic fields — methods: numerical — supernova remnants — X-rays: ISM

1. INTRODUCTION

Some stars have a catastrophic and spectacular death as a supernova (SN) explosion. While the explosion itself takes just a few seconds, the supernova can be observed for years. However, the effects of the explosion (the supernova remnant, SNR) can be observed for tens of thousands of years.

SNRs emit energy over all of the electromagnetic spectrum, but their main "fingerprint" is that they are nonthermal radio sources (showing synchrotron emission). Usually, the synchrotron emission has a shell-like morphology, but this morphology is sometimes not seen at other frequencies.

SNRs can be classified by their shapes or morphologies as shell-like, Crab-like (or plerionic), composite, or thermal X-ray composite. The SNRs of this last type are characterized by having centrally peaked thermal X-ray emission, while at the same time having a shell-like morphology at radio frequencies. As examples of this kind of SNR, we can mention W28 (Dubner et al. 2000), W44 (Giacani et al. 1997), and 3C 400.2 (Dubner et al. 1994; Giacani et al. 1998).

Typical models for the adiabatic phase of SNR evolution (Sedov 1959; Chevalier 1982) have been employed to explain some of the characteristics of these astrophysical objects. However, these adiabatic and one-dimensional models predict shell-like morphologies in radio and X-ray emission. Several authors have proposed different physical models in order to explain the centrally peaked X-ray emission from composite SNRs. White & Long (1991) consider a one-dimensional model in which a remnant is expanding in a clumpy interstellar medium. The evaporation of the clumps produces an increase in the central density of the remnant, increasing the X-ray emission of the central region. Other models consider a large-scale gradient for the interstellar medium (ISM) density, which can affect the remnant evolution and produce SNRs with nonspherical shapes. Together with projection effects (on the plane of the sky), these models could explain the strange morphologies of some remnants at radio and X-ray frequencies (Hnatyk & Petruk 1999; Petruk 2001).

Another mechanism that has been suggested for explaining the centrally peaked X-ray emission in some SNRs is electron thermal conduction. Cox et al. (1999) and Shelton et al. (1999) include isotropic thermal conduction in order to successfully model the X-ray emission from W44. However, if a magnetic field is present, the thermal conduction occurs almost exclusively in the direction parallel to the B field. Zhekov & Myasnilov (2000) have computed models of interacting stellar winds in which they include an approximate calculation of the anisotropic electron thermal conduction. In their simulations, the anisotropic conduction leads to a breakdown of the initial spherical symmetry of the flow.

In the present work, we present two-dimensional, axisymmetric numerical simulations of the evolution of SNRs, in which the anisotropic thermal conduction has been included. The magnetic field configuration is computed explicitly, but the Lorentz force has not been included (so that the magnetic field only affects the properties of the flow through the anisotropic conduction). From our models, we have generated simulated X-ray maps, which could be compared with new observations obtained with X-ray satellites such as *Chandra*, *XMM-Newton*, *ROSAT*, and other satellites. We have also computed radio continuum maps. Finally, we compare our X-ray and synchrotron maps with observations of W44, SN 1006, and G296.5+10.0.

2. THEORETICAL BACKGROUND AND NUMERICAL SIMULATIONS

2.1. *Initial Conditions and Assumptions*

The axisymmetric simulations were carried out with the Yguazú-a code, which is described below. In our models, we

have included a magnetic field, which is initially homogeneous (in modulus and direction). The Lorentz force of the magnetic field on the gas has not been included.

We have then integrated the cylindrically symmetric gas dynamics equations, the induction equation for the magnetic field, and a series of rate equations for different atomic/ionic species. A six-level binary adaptive grid with a maximum resolution of 2.34×10^{17} cm was employed in a 40×40 pc (axial $\times$ radial) computational domain.

In order to test our code (including thermal conduction effects), we have carried out calculations with the parameters of the model of W44 developed by Shelton et al. (1999) and Cox et al. (1999).

The initial remnant is modeled as a sphere, with a radius of 1.5 pc and a total mass of 5 $M_{\odot}$, centered on the origin of the (x, r) coordinate system. We do not employ the self-similar Sedov solution for initializing the density, temperature, and velocity profiles, because this solution is not valid if thermal conduction is taken into account. Instead, the density was considered uniform within the initial remnant, while the velocity profile was modeled as a linear ramp as a function of radius, with a maximum velocity of 5000 km s^{-1} at the outer edge of the remnant. The total initial explosion energy was of 10^{51} ergs, which is split into kinetic and thermal energies. The material within the initial remnant is assumed to be fully ionized.

The magnetic field within and outside this sphere is assumed to be initially parallel to the symmetry axis and to have the same value as in the surrounding medium (which we set to 1 μG, although the actual adopted value does not affect the results from the simulations). Although this initial configuration for $\boldsymbol{B}$ is not realistic, it does not affect the results obtained, as the magnetic field is rapidly advected outward, forcing it to take the configuration appropriate for an expanding hot gas bubble.

With respect to the interstellar medium where the SNR is evolving, we have carried out numerical simulations in two scenarios. In the first one, we studied the evolution of a remnant expanding into an uniform and neutral (except for C, which is singly ionized) environment with a density $n_0 =$ 6 cm^{-3} and a temperature of 1000 K . In the second scenario, the ISM has an exponential density profile (in the x-direction) given by

$$n = n_0 e^{-x/H}, \tag{1}$$

where $H = 22$ pc is the scale height. For these two environments, we have considered the isotropic, anisotropic, and no thermal conduction cases, and their effects on the remnant evolution and X-ray emission.

2.2. *The Yguazú-a Code*

We have employed an axisymmetric version of the Yguazú-a adaptive grid code, which is described in detail by Raga, Navarro-González, & Villagrán-Muniz (2000). This code has been tested with laser laboratory explosions (Sobral et al. 2000; Velázquez et al. 2001a) and jets (Raga et al. 2001), giving confidence in the accuracy of the results obtained when computing SNR models (Velázquez et al. 2001b).

In this code, the gasdynamics equations are integrated with a second-order accurate (in space and time) implementation of the "flux-vector splitting" algorithm of Van Leer (1982), together with a system of rate equations for atomic/ionic species, which are used for computing a nonequilibrium cooling function (a parametrized cooling rate being applied for the high-temperature regime). Rate equations for H I–II, He I–III, C II–IV, and O I–III are considered. The reaction and cooling rates that have been included are described in detail in the Appendix of Raga et al. (2002). In Figure 1, we show the time-dependent cooling function for a parcel that cools at a constant (atom+ion) number density $n = 1$ cm^{-3} from an initial temperature of 10^6 K. This curve compares well with the equivalent cooling function presented by Innes (1985, who includes a considerably more extended ionization network). Furthermore, we have tested the effect of the dust cooling (given by Ostriker & Silk 1973; also Dwek 1981) by adding the cooling due to dust grains in our cooling function. We conclude that the dust cooling could be important for the evolution of young SNRs (with central temperatures larger than 10^8 K), but has little effect on either the evolution or the X-ray emission from old remnants, such as those shown in our models. For this reason, we have neglected the effects of dust cooling in our calculations. We also note that we have thermal equilibrium between electrons and ions, so that the gas can be described by a single temperature.

In this code, we have included the induction equation for the magnetic field. In cylindrical coordinates, this equation takes the form

$$\frac{\partial B_x}{\partial t} + \frac{\partial}{\partial r}\left(B_x v - B_r u\right) = -\frac{B_x v - B_r u}{r}, \tag{2}$$

$$\frac{\partial B_r}{\partial t} - \frac{\partial}{\partial x}\left(B_x v - B_r u\right) = 0 \tag{3}$$

for the axial (B_x) and radial (B_r) components of the magnetic field. In equations (2) and (3), u and v are the axial and radial components of the flow velocity, respectively.

These equations are integrated with a simple, centered-difference scheme, which is marched forward in time with the same "half step/full step" time-stepping scheme that is used for the gasdynamics equations (see Raga et al. 2000). The magnetic field is assumed to be weak enough so that the Lorentz force is negligible. However, the field interacts with the flow through anisotropic thermal conduction. This is described in § 2.3.

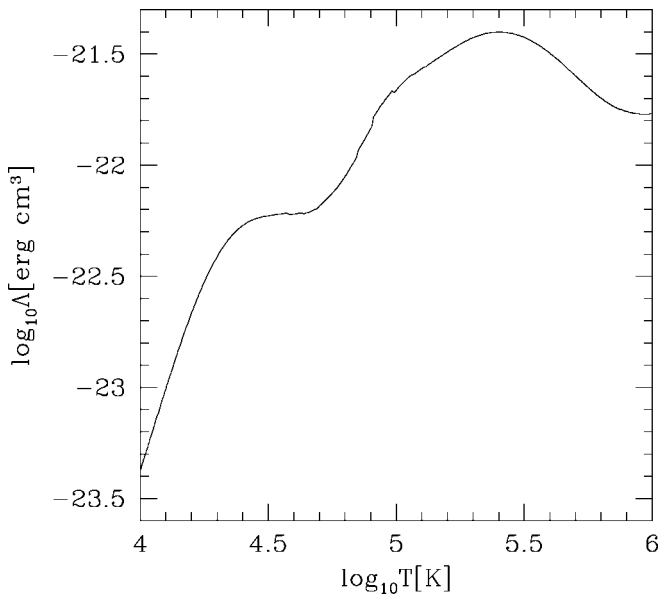

FIG. 1.—Cooling curve obtained with cooling functions included in the Yguazú-a code.

2.3. *Thermal Conduction Treatment*

In the absence of a magnetic field, the heat flux for classical electronic thermal conduction is proportional to the temperature gradient ∇T, and is written as

$$q_c^e = -\kappa \nabla T, \tag{4}$$

where the thermal conductivity is $\kappa = \beta T^{5/2}$, with $\beta \simeq 6 \times 10^{-7}$ ergs s^{-1} K^{-1} cm^{-1} (for a fully ionized plasma, Spitzer 1962). When a magnetic field $\boldsymbol{B}$ is present, the thermal conduction is anisotropic, since the characteristic transport lengths along and across the magnetic field are different; the former is the electron collisional mean free path λ_e, whereas the latter is the electron gyroradius ρ_e. Usually, $\lambda_e \gg \rho_e$, and thus only the component of the heat flux parallel to the magnetic field is important, which has an expression analogous to equation (4):

$$q_{\parallel}^e = -\kappa_{\parallel}^e \nabla_{\parallel} T, \tag{5}$$

where $\nabla_{\parallel} T = [(\hat{\boldsymbol{B}} \cdot \nabla) T] \hat{\boldsymbol{B}}$ is the temperature gradient parallel to the magnetic field. The more accurate expression for the parallel thermal conductivity is (Braginskii 1965)

$$\kappa_{\parallel}^e = 3.2 \frac{nk^2 T \tau_e}{m_e}, \tag{6}$$

where n is the electron number density, k is the Boltzmann constant, m_e is the electron mass,

$$\tau_e = 0.275 \frac{T_e^{3/2}}{n\Lambda} \text{ s}, \tag{7}$$

is the electron collision time, and $\Lambda = 24 - \ln(n^{1/2} T^{-1})$ is the Coulomb logarithm for electron-electron collisions.

However, the classical expression for the heat flux of equation (4) is no longer valid when λ_e is larger than the temperature scale height $L_T = T/|\nabla T|$. In this case, the collisions are not relevant for producing the energy transport, and the heat is advected at the electron free streaming velocity, which is of the order on the electron thermal speed. This saturated heat flux has been investigated by Cowie & McKee (1977), who have found that, in the absence of a magnetic field, it can be written as

$$q_{\text{sat}} = -5 \phi_s c P \hat{\boldsymbol{T}}. \tag{8}$$

In equation (8), $c = (P/\rho)^{1/2}$ is the isothermal sound speed, P is the gas pressure, ϕ_s is an adimensional coefficient (of order 1), and $\hat{\boldsymbol{T}}$ indicates the direction of the temperature gradient. In presence of a magnetic field, the saturated flux is analogous to equation (8) with the difference that the flux direction is along the magnetic field, taking the form

$$q_{\parallel,\text{sat}} = -\text{Sgn}(\boldsymbol{B} \cdot \nabla T) 5 \phi_s c P \hat{\boldsymbol{B}}. \tag{9}$$

If the SNR gas temperature is very high ($T > 10^{10}$ K), equations (8) and (9) would give superluminal speeds for the flux, which is not relativistically correct, so a light speed cutoff is included in the sound speed to stop this from happening.

In the following sections, we present simulations of SNRs with and without thermal conduction. We consider both isotropic and anisotropic heat fluxes, given by equations (4) and (5), respectively, when $\lambda_e < L_T$, and by equations (8) and (9), respectively, when $\lambda_e > L_T$.

2.4. *Simulation of X-Ray and Synchrotron Emission*

In order to analyze the effects of thermal conduction (isotropic and anisotropic cases) on the observational properties of SNRs, we have generated simulated X-ray and radio continuum (synchrotron) emission maps.

The simulated X-rays maps can be directly compared with observations obtained (for example) with the *Chandra* satellite. For this, we have integrated the X-ray emission coefficient over the 0.3–10 keV photon energy range. We have also integrated the X-ray coefficient over the soft (0.3–2.1) and hard (2.1–10 keV) bands of the *Chandra* satellite. Finally, we have added the effects of the interstellar extinction for the 0.3–10 keV photon energy range with the extinction curve of Morrison & McCammon (1983).

For the X-ray emission, we have assumed that the gas is in coronal ionization equilibrium. This is clearly an approximation, as the ionization state of the high temperature region of the remnant is probably not in equilibrium (Benjamin, Benson, & Cox 2001). For the calculation of the emission, we have used the coronal ionization equilibrium of Mazzotta et al. (1998) and Landini & Monsignori Fossi (1991), used solar abundances, and assumed that all of the excitation is in the low-density regime (i.e., that the emission coefficient is proportional to the square of the density n).

For computing the emission coefficient, $j_\nu(n,T)$, we have employed the CHIANTI[1] atomic database and its associated IDL software (Dere et al. 2001; Young et al. 2003). With the CHIANTI routines, we generate the synthetic X-ray emission coefficient (integrated over the energy range of interest) as a function of temperature T for a given density, and then scale it with the $j \propto n^2$ low-density regime density dependence.

The synchrotron emission can be calculated as (Clarke, Burns, & Norman 1989; Jun & Norman 1996)

$$i(\nu) \propto \rho^{1-2\alpha} P^{2\alpha} (B \sin\psi)^{\alpha+1} \nu^{-\alpha}, \tag{10}$$

where ρ is the density, P is the pressure, B is the intensity of the magnetic field, α is the spectral index parameter, ν is the frequency, and ψ is the angle between the plane of the sky and the direction of the magnetic field.

Figure 2 shows the coordinate system employed for simulating the radio emission. In this figure, the $x'y'$-plane is the plane of the sky, $\hat{\boldsymbol{x}}$ is the symmetry axis (which is parallel to the initial direction of the magnetic field), ϕ is the angle between the symmetry axis and the plane of sky, and θ is the polar angle (which lies on the yz-plane). Considering this configuration and fixing the frequency ν, equation (10) can be rewritten as

$$i(\nu) \propto \rho^{1-2\alpha} P^{2\alpha} (B_x \sin\phi + B_r \sin\theta \cos\phi)^{\alpha+1}. \tag{11}$$

For all synchrotron emission maps, we have assumed an $\alpha = 0.5$ spectral index, which is a typical value for SNRs. The corresponding emission coefficients are then integrated through lines of sight in order to obtain the X-ray and synchrotron emission maps.

[1] The CHIANTI database and its associated IDL procedures are freely available at http://wwwsolar.nrl.navy.mil/chianti.html, http://www.arcetri.astro.it/science/chianti/chianti.html, and http://www.damtp.cam.ac.uk/users/astro/chianti/chianti.html.

3. RESULTS

For each of our two ISM scenarios (one with uniform density and the other with an exponential density gradient), we have computed three models with the parameters described in § 2.1, considering anisotropic conduction, isotropic conduction (see § 2.3), and no conduction.

For the first scenario, in Figure 3, we show the direction of the magnetic field for the isotropic, anisotropic, and no conduction cases (top, center, and bottom, respectively). In the three cases, the magnetic field remains parallel to the symmetry axis only in the region close to the axis, but it becomes almost parallel to the SNR shock over most of the volume of the remnant. The magnetic field lines produce a "lid" that limits the thermal conduction only to the region close to the symmetry axis (this effect is considered correctly only in the "anisotropic conduction model" shown in the central panel of Fig. 3). From this figure, it is also observed that the SNR radius is similar for the three cases, i.e., thermal conduction only affects the internal SNR structure and not the evolution of the outer shock wave.

From the numerical results and following the assumptions and equations of § 2.4, we have simulated X-ray and synchrotron maps, which we describe below.

3.1. *X-Ray Emission Maps*

3.1.1. *Expansion into a Uniform Environment*

For the case of a remnant expanding into an ISM with uniform density, we have carried out numerical simulations considering the effects of isotropic, anisotropic, and no thermal conduction.

As a first step in this study, we focus on the isotropic conduction case. Figure 4 shows simulated X-ray maps for a $t = 21,000$ yr integration time. The panels of Figure 4 show the X-ray emission maps over photon energy ranges (in keV) of 0.3–10 (*top left*), 0.3–2.1 (soft X-ray emission, *top right*), 2.1–10 (hard X-ray emission, *bottom left*), and 0.3–10 with extinction (*bottom right*). These maps were obtained by integrating the X-ray emission coefficient along the lines of sight.

In Figure 4, we see that the top panels exhibit quite similar shell-like structures. However, when the remnant is observed in the hard X-ray band, the morphology of the X-ray emission changes drastically to become centrally peaked (Fig. 4, *bottom right*). Actually, in real X-ray observations, the extinction effect (produced by the foreground ISM) is present. In order to make a more realistic comparison between observations and our simulated maps, we have considered how the foreground extinction modifies the shape of the simulated X-ray maps. The result can be observed in the bottom right panel. Again, we have considered the complete photon energy range of 0.3–10 keV, but we have now included the extinction produced by the ISM for an H I column density of 1.8×10^{22} cm^{-2} (Rho et al. 1994) in computing the X-ray emission map. For these calculations, we have considered the frequency-dependent

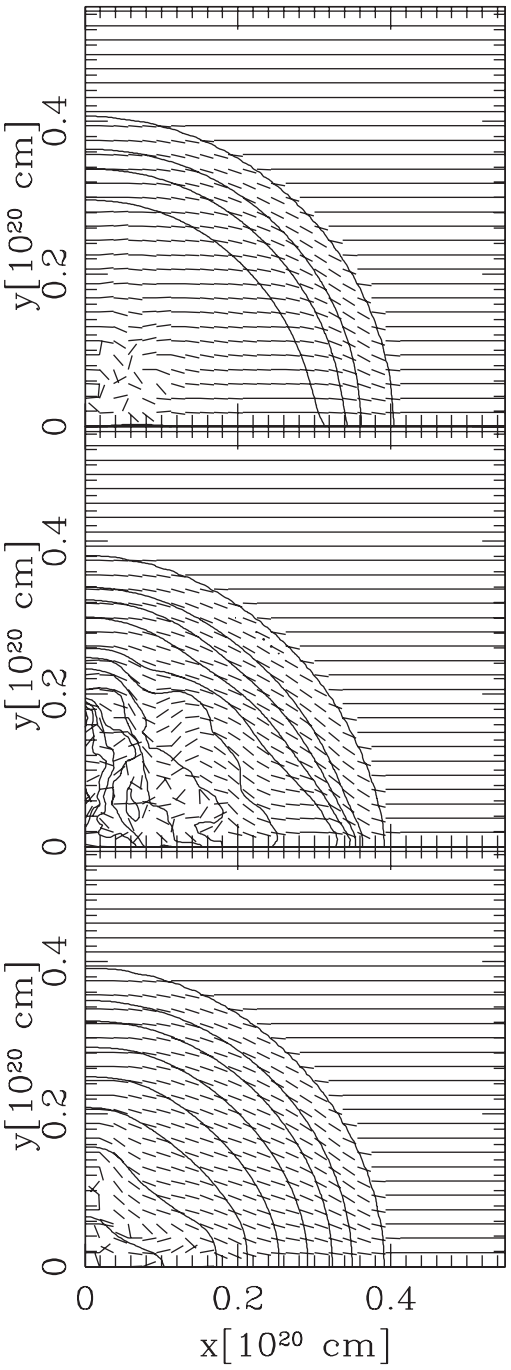

FIG. 3.—Magnetic field direction at 21,000 yr of the SNR evolution for the isotropic, anisotropic, and no thermal conduction cases (*top to bottom*, respectively), represented by short line segments. The $\sqrt{2}$, logarithmic contours represent the density stratification.

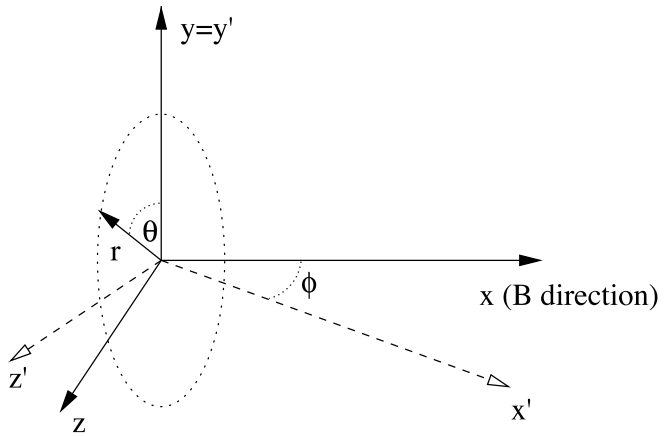

FIG. 2.—Scheme of the coordinate system employed for simulating synchrotron emission. The x-axis is the symmetry axis (coinciding with the initial magnetic field direction). The plane of the sky is the $x'y'$-plane. The z'-axis is the line of sight.

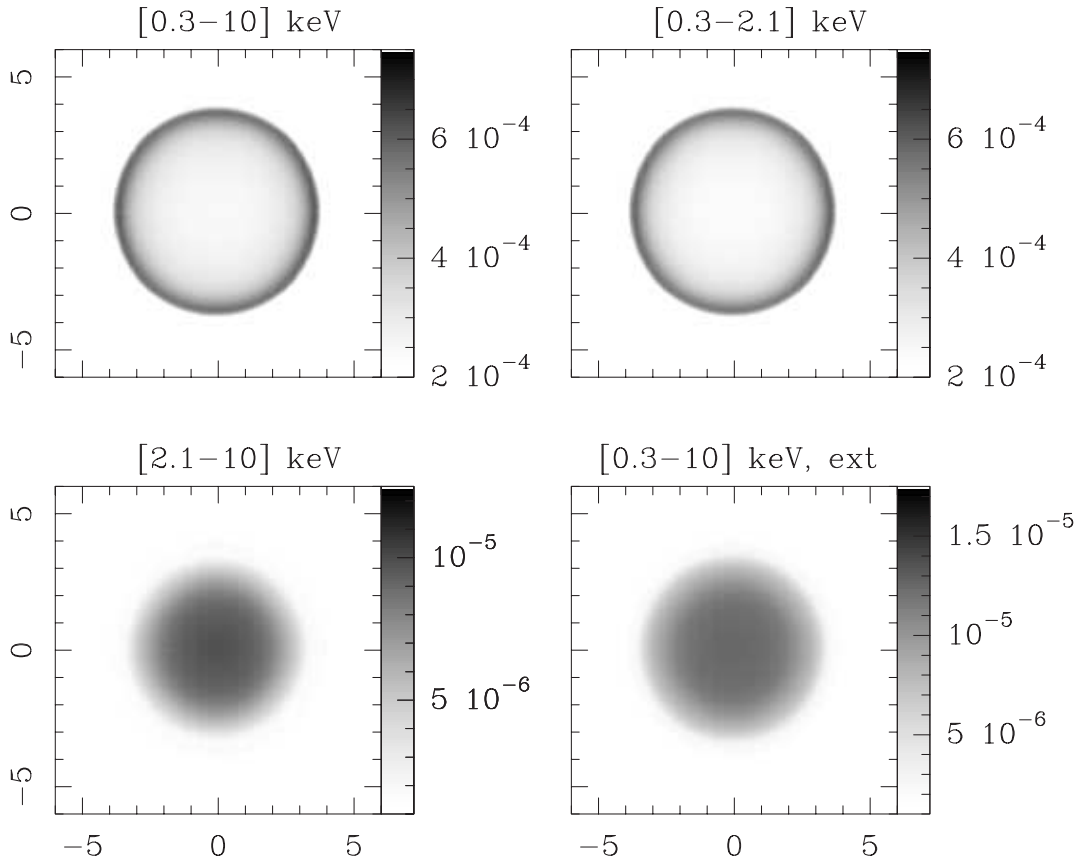

FIG. 4.—Simulated X-ray maps at a $t = 21,000$ yr integration time for the isotropic conduction case, when the SNR is expanding in an uniform ISM. A $\phi = 0^\circ$ angle between the symmetry axis and the plane of the sky has been considered. *Top left*: X-ray emission for a photon energy range of 0.3–10 keV (the total energy range of *Chandra*). *Top right*: Emission in the soft X-ray band (0.3–2.1 keV). *Bottom left*: Simulated image obtained for hard X-rays (2.1–10 keV). *Bottom right*: Simulated X-ray emission for the 0.3–10 keV energy range, after applying a foreground extinction correction (see text). Centrally peaked morphologies for X-ray emission are obtained in the two bottom panels. In all figures, the linear gray scales are given by the bars on the right of each panel (in units of ergs s^{-1} cm^{-2} sr^{-1}), while the x- and y-axes are labeled in units of 10^{19} cm.

extinction of Morrison & McCammon (1983). In this case, the simulated X-ray emission shows a centrally peaked morphology similar to the morphology obtained for the hard X-ray band image.

Such centrally peaked configurations have been obtained in the past by Cox et al. (1999) and Shelton et al. (1999), who carried out a numerical study considering isotropic thermal conduction. They simulated X-ray emission for the *ROSAT* X-ray band, modeling the X-ray emission from W44.

It is interesting to compare how simulated X-ray emission maps change if isotropic, anisotropic, and no thermal conduction are considered. This comparison is made in Figure 5. The isotropic, anisotropic, and no conduction cases are shown in the top, center, and bottom rows, respectively. The X-ray emission of all these maps corresponds to the photon energy range of 0.3–10 keV and has been corrected for foreground extinction (as described above). These maps correspond to a $t = 21,000$ yr integration time. This figure also shows how projection effects modify the X-ray distribution in the simulated emission maps. The X-ray images obtained with projection angles $\phi = 0^\circ$, 45°, and 90° (ϕ being the angle between the plane of the sky and the symmetry axis, which is given by the initial magnetic field direction) are displayed in the left, central, and right columns of Figure 5, respectively.

As expected, we find that there is no dependence of the emission on the value of ϕ for either the isotropic or the no conduction cases. While the isotropic thermal conduction case produces a centrally peaked X-ray emission map (as discussed above), the morphology of the X-ray emission for the no conduction case is of the shell-like type (Fig. 5, *bottom*).

Differences between the emission for different values of ϕ are observed for the anisotropic thermal conduction case (Fig. 5, *central row*). At an angle $\phi = 0^\circ$, the remnant exhibits a double-shell X-ray morphology. The emission from the outer shell is stronger than the emission from the inner shell. Both shells are fainter on the symmetry axis. For $\phi = 45^\circ$, two minima are observed, symmetrically situated between both shells, along the x-axis. An axially symmetric double-shell morphology with a central minimum is obtained for $\phi = 90^\circ$.

Finally, another effect of the thermal conduction on the X-ray emission is to increase the total X-ray luminosity. We obtain luminosities $L_X = 123$, 60, and 47 $L_\odot$ for the isotropic, anisotropic, and no thermal conduction cases, respectively.

3.1.2. *Expansion into an Environment with an Exponential Density Profile*

Cox et al. (1999) and Shelton et al. (1999) carried out numerical simulations in order to explain the X-ray emission from W44. They considered that the environment around this remnant has an exponential density stratification (see eq. [1]). Following these authors, we have computed models with such an environmental stratification.

Figure 6 shows the X-ray emission maps for the isotropic (*top*), anisotropic (*center*), and no conduction (*bottom*) cases

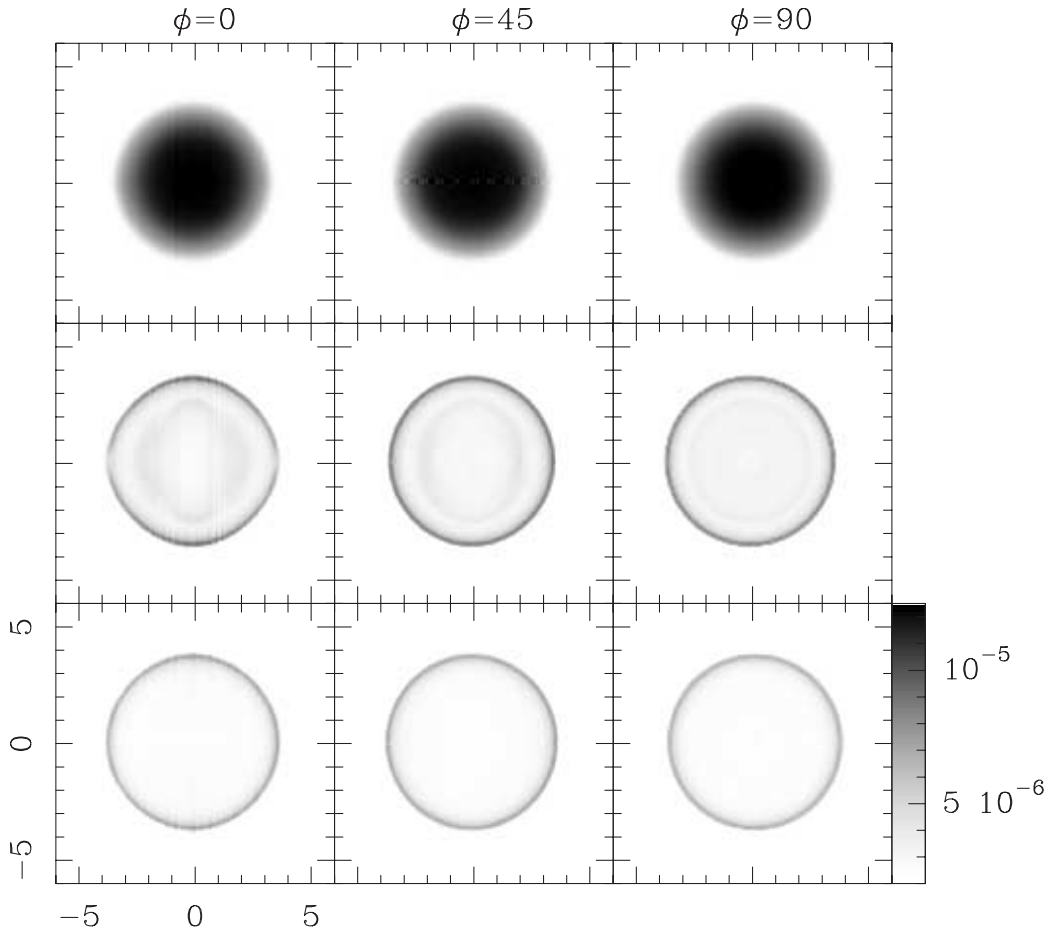

FIG. 5.—Simulated X-ray maps for a remnant expanding into an uniform ISM, corresponding to a $t = 21,000$ yr integration time. *Top*: X-ray emission for the isotropic conduction case with angles respect to the plane of the sky of 0° (*left*), 45° (*central*) and 90° (*right*). *Center*: Simulated X-ray maps for the anisotropic conduction case. *Bottom*: X-ray emission for the no conduction case. All panels show X-ray emission in the 0.3–10 keV energy range, after doing the foreground extinction correction. Gray scales are linear and are given by the bars on the right (in units of ergs s^{-1} cm^{-2} sr^{-1}), while the *x*- and *y*-axes are labeled in units of 10^{19} cm.

at $t = 21,000$ yr, but for a remnant that evolves into an ISM with an exponential density stratification (along the *x*-axis). The density decreases in the positive *x*-direction. Three different orientation angles have been considered. In all cases, we have considered the energy range of 0.3–10 keV, and the X-ray emission is corrected for the foreground ISM extinction.

The simulated X-ray maps for the anisotropic conduction case (Fig. 6, *central row*) exhibit diffuse central emission with a strong partial outer shell. The outer shell has a differentiated emission distribution with stronger emission on the left (see $\phi = 0^\circ$ and 45°), in the direction toward the high density region. When the SNR is observed at $\phi = 90^\circ$, the X-ray emission is centrally peaked. This central emission is surrounded by a weak, thin shell. For the no conduction case, the X-ray morphology is quite similar to the anisotropic case, with the difference that it is not centrally peaked at $\phi = 90^\circ$. For $\phi = 0^\circ$ and 45°, strong arclike emission is observed in the east, and a complete shell is obtained for $\phi = 90^\circ$.

3.2. *Synchrotron Emission Maps*

Figure 7 shows the synchrotron emission maps computed for a SNR expanding into an uniform ISM, for a $t = 21,000$ yr integration time. We have consider the isotropic, anisotropic, and no thermal conduction cases. This figure shows the maps obtained for a $\phi = 45^\circ$ and $\phi = 0^\circ$ angle between the symmetry axis and the plane of the sky (*right and left, respectively*). All of the maps show "incomplete shell" morphologies, since the synchrotron emission coefficient depends on the angle between the magnetic field and the line of sight (see eq. [11]).

It is interesting that, for the three models, we obtain two arclike features with two intensity peaks centered on the symmetry axis for the $\phi = 45^\circ$ maps and four arclike features for the $\phi = 0^\circ$ maps (Fig. 7). On the other hand, the X-ray emission of the anisotropic conduction model (Fig. 5) shows two ridges with "holes" along the symmetry axis (at $\phi = 0^\circ$). This general morphology is seen in X-ray maps with a large range of different values of the orientation angle ϕ. Therefore, our models predict that one should see morphologically different structures of arclike ridges in the synchrotron and in the X-ray maps of a given object.

There are some SNRs that have this kind of morphology in X-ray and radio emission and are called "barrel-like" SNRs. These SNRs are characterized by a clear axis of symmetry, a low level of emission along this axis, and two bright limbs on either side. In § 3.3.2, we compare our numerical results with observations of two remnants that belong to this group.

3.3. *Comparison with Observations*

3.3.1. *W44*

W44 is an example of a composite SNR, which has thermal X-ray emission inside a hollow radio shell. Figure 8 (*left*)

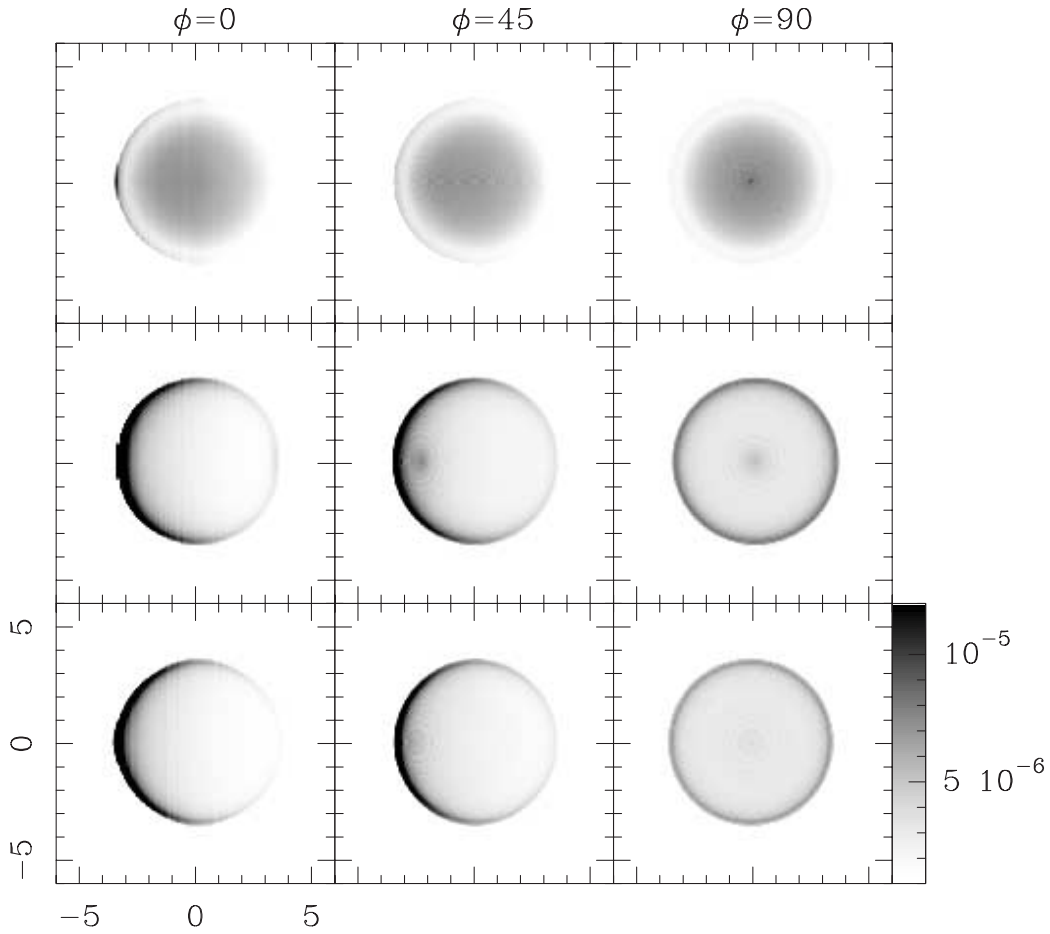

FIG. 6.—As Fig. 5, but for the model in which the SNR is evolving into a stratified ISM. The X-ray emission in the energy range 0.3–10 keV (after carrying out an extinction correction) for the isotropic, anisotropic, and no conduction cases, are shown in the top, center, and bottom panels, respectively. The angles indicate the orientation with respect to the plane of the sky. The *x*- and *y*-axes are labeled in units of 10^{19} cm. The X-ray emission is shown with a linear gray scale in units of ergs s^{-1} cm^{-2} sr^{-1}, given by the bar.

shows a gray-scale image of W44 at 1.4 GHz from Giacani et al. (1997). This radio image was obtained after reprocessing VLA[2] archive data in the C and D configurations and adding the short-spacing contribution from single-dish observations. The resulting synthesized beam width is 15″ and the resulting noise level is 12 mJy $beam^{-1}$. The data processing is described in Giacani et al. (1997). This high-resolution image shows an elongated shell of about $34' \times 24'$ in size, with numerous knots and filamentary arcs of synchrotron radiation, both in the interior and along the perimeter of W44. Figure 8 (*right*) shows the radio emission at 1.4 GHz (*contours*) superposed on a gray-scale representation of the *ROSAT* X-ray emission (taken from Rho et al. 1994). The brightest soft X-ray emission is concentrated toward the center of the remnant, where it has a knotty and irregular distribution. Diffuse X-ray emission extends beyond the central region to the north where it matches the radio edge.

Our models incorporating isotropic thermal conduction can explain the centrally peaked thermal X-ray emission together with a shell-type radio morphology for a SNR such as W44. Our results are in good agreement with those of Shelton et al. (1999) and Cox et al. (1999). However, the models of Shelton et al. (1999) and Cox et al. (1999) and our model for the isotropic thermal conduction predict an almost spherical central X-ray emission, while in the W44 case, this emission has an ellipsoidal shape. On the other hand, when we consider the anisotropic thermal conduction model, the resulting morphology for the X-ray emission is no longer centrally peaked, such as that observed in Figure 6.

3.3.2. *Barrel-like SNRs: the Remnant of SN 1006 and G296.5+10.0*

As mentioned in § 3.2, our simulated radio continuum maps give arclike emission features for all models. This arclike morphology is also observed in the simulated X-ray emission maps for the model of a remnant expanding into an uniform ISM, which considers anisotropic thermal conduction (orientation angle $\phi = 0^\circ$, Fig. 5, *left center*).

This "barrel-like" morphology for both radio and X-ray emission is observed in some Galactic SNRs. Two examples are the remnant of SN 1006 and G296.5+10.0 (also PKS 1209−52).

The remnant of SN 1006 is a young remnant with an angular size of approximately 30′. Figure 9 (*left*) shows, in gray scale and contours, the radio image at 4.85 GHz (obtained from the survey of Condon, Broderick, Seielstad 1991, 1993, 1994, by means of the SkyView Advanced form facility[3]),

[2] The Very Large Array of the National Radio Astronomy Observatory is a facility of the National Science Foundation operated under cooperative agreement by Associated Universities, Inc.

[3] See http://skyview.gsfc.nasa.gov/cgi-bin/skvadvanced.pl.

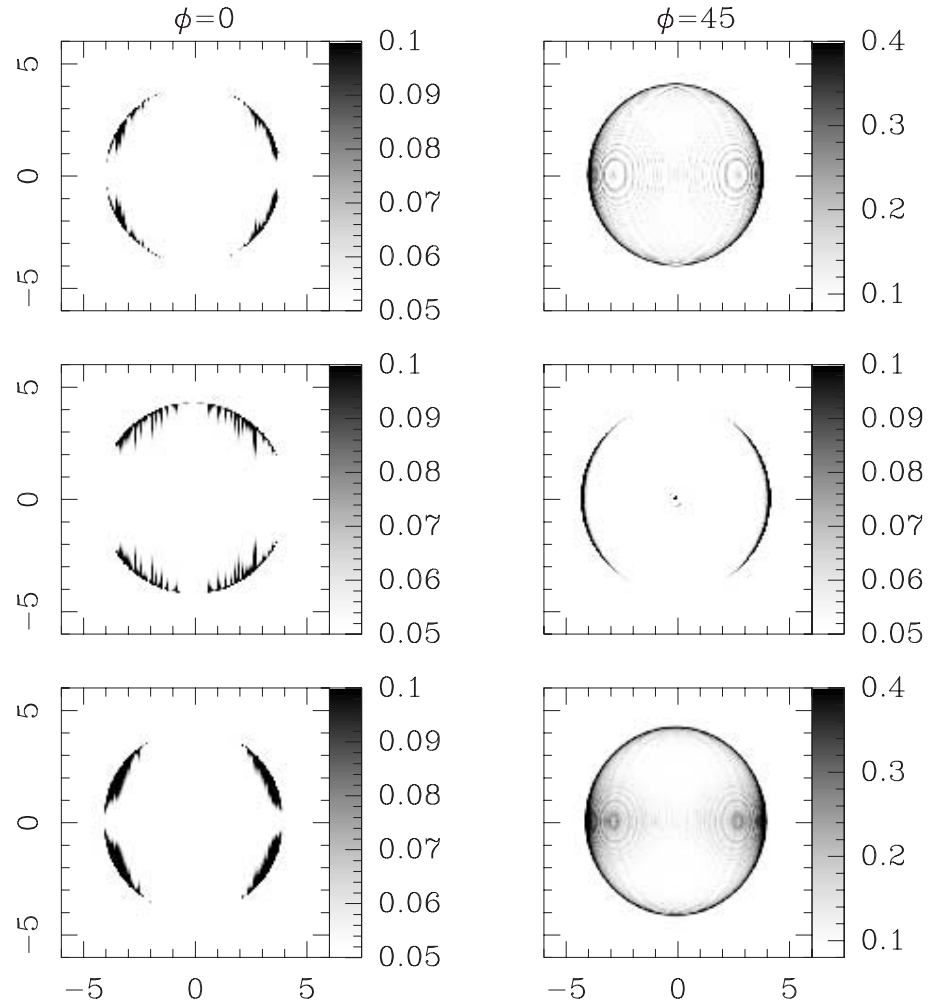

FIG. 7.—Synchrotron emission at a $t = 21,000$ yr time for a remnant expanding into an uniform ISM. The isotropic, anisotropic, and no thermal conduction cases are shown in the top, central, and bottom panels, respectively. *Left*: Radio continuum emission when the angle with respect to the plane of the sky is $\phi = 0^{\circ}$. *Right*: Emission for $\phi = 45^{\circ}$. Gray scales are linear and are given by the bars on the right, in arbitrary units.

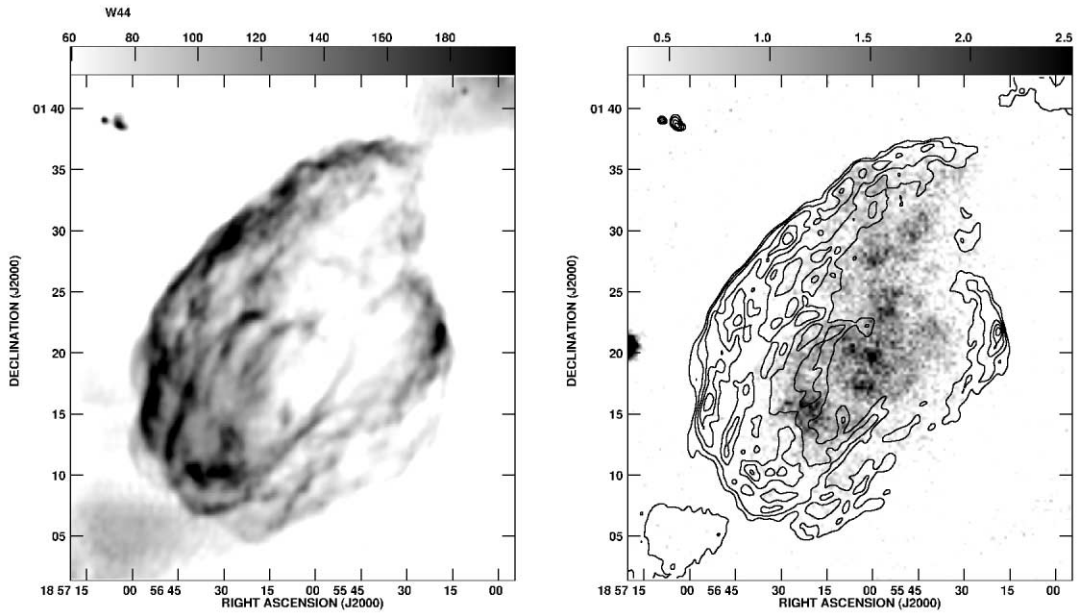

FIG. 8.—*Left*: Gray-scale image of W44 at 1.4 GHz, obtained with the VLA (Giacani et al. 1997). The synthesized beam is 15″. The gray scale corresponds to the range 60–200 mJy beam^{-1}. *Right*: Overlay of the X-ray emission (*grays*; Rho et al. 1994) and radio continuum at 1.4 GHz (*contours*) of W44. The gray scale range (*horizontal bar*) is 0.3–2.5 counts s^{-1} pixel^{-1}. The radio contours are at 90, 120, 160, 200, and 240 mJy beam^{-1}.

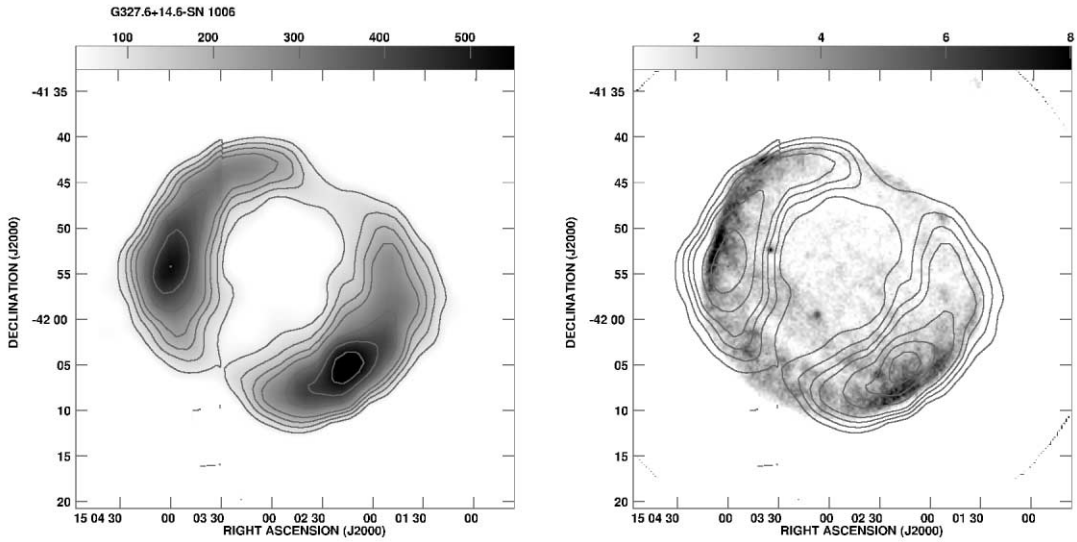

FIG. 9.—*Left*: Radio image of the SNR of SN 1006, obtained from the survey at 4.85 GHz (Condon et al. 1991, 1993, 1994). The gray scale corresponds to the range 40–550 mJy beam^{-1}, and the resolution is 7′. The contours are 80, 130, 180, 230, 330, 430, and 530 mJy beam^{-1}. *Right*: Overlay of the *ROSAT* image of this remnant (*grays*) and radio continuum (*contours*). The gray-scale range is 1–8 counts s^{-1} pixel^{-1}.

with an angular resolution of 7′. Figure 9 (*right*) is an overlay of the X-ray emission (*gray scale*, obtained from *ROSAT* archival data) and radio contours at 4.85 GHz. Both in the radio and X-ray regimes, SN 1006 has a barrel-like appearance with two symmetric, bright limbs (toward the northeast and southwest) and almost no emission at the sites where the axis of symmetry intersects the SN shell.

Willingale et al. (1996), Winkler & Long (1997), and Allen, Petre, & Gotthelf (2001) carried out studies of the X-ray emission from this remnant, by means of observations obtained with *ASCA*, *ROSAT*, and other satellites. They found that the X-ray emission from this SNR has both nonthermal and thermal components. The nonthermal emission is observed forming the rims, while thermal X-ray emission is detected from the interior of the SNR. We can qualitatively reproduce the morphology in both radio and X-rays when we consider a model in which the SNR is expanding into an uniform medium. This assumption is valid for this source, since observations of the neutral gas in the environs of this remnant have shown that the surroundings of SN 1006 are quite homogeneous (Dubner et al. 2002). However, the simulated thermal X-ray emission resulting from our model is not adequate for explaining the nature of the bright arcs observed in SN 1006.

G296.5+10.0 is another example of a barrel-like SNR, at both radio and X-ray wavelengths. This remnant is evolved and the angular size in the north-south–direction is about 80′, 1.6 times the diameter in the east-west–direction. The radio map at 4.85 GHz (obtained from Condon et al.'s 1991, 1993, 1994 surveys) has an angular resolution of 7′ and is shown in Figure 10 (*left*). This radio image shows two bright arcs toward

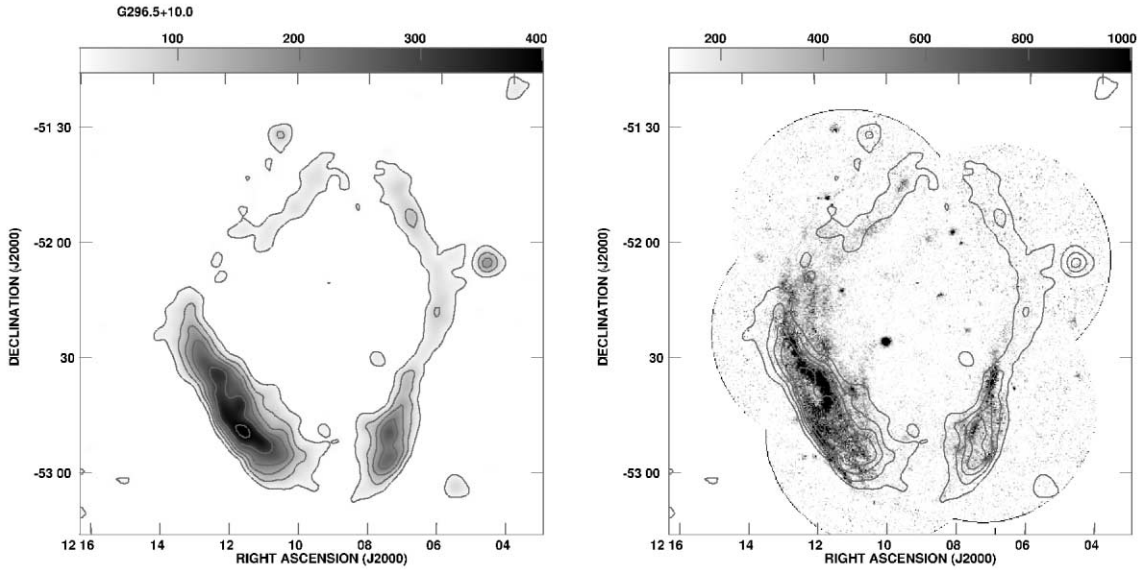

FIG. 10.—Same as Fig. 9, but for the emission of G296.5+10.0. *Left*: Synchrotron emission at 4.85 GHz (Condon et al. 1991, 1993, 1994), in the range 20–400 mJy beam^{-1} and with an angular resolution of 7′. The contours correspond to the levels 30, 90, 150, 210, 300, and 400 mJy beam^{-1}. *Right*: X-ray emission (*grays*) of this SNR, corresponding to the range 0.1–1 $\times$ 10^{-3} counts s^{-1} pixel^{-1}, while the contours represent the emission at 4.85 GHz.

the east and the west. The eastern arclike feature looks broken and has strong emission to the southeast. The western arc looks almost complete. The distribution of the X-ray emission has similar appearance (see the overlay of X-ray and radio contours in Fig. 10, *right*) to that observed in radio frequencies. A bright compact X-ray source (1E 1207.4−5209) located at 6′ from the geometrical center of the remnant has no radio counterpart and is classified as a radio-quiet neutron star.

Several studies of the extended emission and the central sources have shown that the X-ray arclike features are of thermal origin (Matsui, Long, & Tuohy 1988; Mereghetti, Bignami, & Caraveo 1996; Zavlin et al. 2000). Radio continuum polarization studies at 2.4, 4.8, and 8.4 GHz revealed that this remnant has a well-defined magnetic field (Milne & Haynes 1994), which is tangential to the bright arclike features. On the other hand, Giacani et al. (2000), by means of an HI study, found that this remnant is expanding into an almost uniform ISM.

Taking into account these observational results, our model for the anisotropic thermal conduction of a remnant evolving in an uniform medium (in agreement with the work of Giacani et al. 2000) could qualitatively explain the characteristics of the radio and X-ray emission of a barrel-like remnant, such as G296.5+10.0. Furthermore, this model produces a tangential magnetic field configuration (Fig. 3, *center*), which agrees with the results obtained from the polarization study of Milne & Haynes (1994).

4. CONCLUSIONS

In this work, we simulate the X-ray and synchrotron emission of a SNR that expands into an homogeneous ISM or evolves in a stratified environment. For both scenarios, we have considered the cases with isotropic, anisotropic, and no thermal conduction. We have also taken into account how projection effects can modify the morphology of the remnant in both the X-ray and the radio continuum emission and the importance of including a dust cooling function. With respect to the latter, we have found that the effects of dust cooling can be neglected in our models.

From our simulations, we see that the thermal conduction has strong effects on the X-ray emission and only rather weak effects on the synchrotron emission (see Figs. 4–7). Up to now, previous studies of the influence of thermal conduction on the X-ray emission had only considered the isotropic conduction case.

For the scenario of a remnant expanding into an uniform density environment, the first important result is that thermal conduction produces an increase in the X-ray emission, resulting in a total X-ray luminosity around 40% larger than in the no conduction case (after carrying out an extinction correction). The morphology of the X-ray emission is centrally peaked for the isotropic conduction case when the remnant is "observed" in the hard X-ray band or when it is "observed" in the complete range of 0.3–10 keV but only after doing the extinction correction. In the case of anisotropic conduction, the X-ray emission can be described as double-shell–like, with a bright outer shell and a faint inner shell. Both shells appear broken for a $\phi = 0^\circ$ projection angle. At $\phi = 45^\circ$, two minima are located on the x-axis between both shells. In the case in which the thermal conduction is not considered, for all angles the X-ray emission has a shell-like morphology, surrounding weak and diffuse central emission.

Shelton et al. (1999) studied the evolution of a remnant moving into ISM with a density gradient. They obtained simulated maps with centrally peaked X-ray morphologies, employing two *ROSAT* energy bands (soft: 0.4–1.56 and hard: 1.05–2.04 keV; see Shelton et al. 1999). From our simulations, we only observe central X-ray emission for the isotropic conduction case at $\phi = 90^\circ$. In the other cases, the X-ray emission has a central "half-moon" morphology, with a large enhancement in X-ray emission in the direction of increasing ISM density (see Fig. 6).

Our anisotropic thermal conduction model does not produce centrally peaked X-ray emission (only for the case of a SNR moving into an ISM with density gradient, a weak central maximum is observed at $\phi = 90^\circ$). Thermal conduction is inhibited by the magnetic field in the region behind the SNR shock wave, where the magnetic field is almost parallel to the SNR shock front (Fig. 3, *center*). Anisotropic thermal conduction seems to "destroy" the centrally peaked morphology of the isotropic conduction case, and the total X-ray luminosity is increased by 20% with respect to the no conduction case.

In the literature, there is an ongoing discussion on the importance of thermal conduction in the presence of magnetic fields. There are two papers that discuss thermal conduction in tangled magnetic fields, for the case of a Galactic cluster. Malyshkin (2001) concluded that thermal conduction is never totally suppressed (but is reduced by a factor of 100 with respect to the Spitzer value). Narayan & Medvedev (2001) find that, for the case of a magnetized plasma with chaotic fluctuations, thermal conduction is very efficient (only 5 times lower than the Spitzer value).

Our numerical simulations develop an internal region of tangled magnetic fields, which is surrounded by a "shell" of ordered fields (see Fig. 4). However, because of the limited spatial resolution of our simulations (and also because they are axisymmetric), the internal "turbulent" region probably does not develop the small-scale structure that would arise in the real high Reynolds number flow. Also, we have not included the ion thermal conduction perpendicular to $\boldsymbol{B}$ (which, in that direction, dominates over the electron conductivity), which, although several orders of magnitude lower than the electron conductivity along $\boldsymbol{B}$, might still have some effect on the structure of the SNR. Because of these uncertainties, our anisotropic conduction simulations should be regarded only as a first attempt to model in some detail the effects of a magnetic field on the thermal conduction within a SNR.

In summary, anisotropic thermal conduction is not an adequate model for describing the characteristics of the X-ray emission from thermal composite SNRs such as W44. Notwithstanding, an anisotropic thermal conduction model seems to be adequate for explaining the morphology of the so-called barrel-like SNRs, an example of which is G296.5+10.0. Isotropic thermal conduction models do produce centrally peaked X-ray emission, but our study shows that it is important to consider an appropriate X-ray energy range and to know the projection angle. It is also necessary to include the foreground extinction correction for calculating the simulated X-ray emission maps. Finally, our models show that the effect of an ordered magnetic field is to strongly reduce the effects of the conduction, therefore calling at least partially into question the validity of the previous isotropic conduction simulations.

We thank Don Cox for his helpful comments on a first version of this paper. We also thank Randall Smith (the referee) for his suggestions that helped to improve a previous

version of this manuscript. A. R. and P. F. V. acknowledge financial support from Conacyt (Mexico) grants 36572-E and 41320-E, and DGAPA (UNAM) grant IN 112602. J. M. is supported by DGAPA (UNAM) grant IN 116200. E. B. G. acknowledges financial support by UBACYT (Argentina) grant A013. We also acknowledge Israel Díaz for maintaining and supporting our multiprocessor Linux server on which we have carried out our numerical simulations.

REFERENCES

Allen, G. E., Petre, R., & Gotthelf, E. V. 2001, ApJ, 558, 739
Benjamin, R. A., Benson, B. A., & Cox, D. P. 2001, ApJ, 554, L225
Braginskii, S. I. 1965, Rev. Plasma Phys., 1, 205
Chevalier, R. 1982, ApJ, 258, 790
Clarke, D. A., Burns, J. O., & Norman, M. L. 1989, ApJ, 342, 700
Condon, J. J., Broderick, J. J., & Seielstad, G. A. 1991, AJ, 102, 2041
Condon, J. J., Broderick, J. J., Seielstad, G. A., Douglas, K., & Gregory, P. C. 1994, AJ, 107, 1829
Condon, J. J., Griffith, M. R., & Wright, A. E. 1993, AJ, 106, 1095
Cowie, L. L., & McKee, C. F. 1977, ApJ, 211, 135
Cox, D. P., Shelton, R. L., Maciejewski, W., Smith, R. K., Plewa, T., Pawl, A., & Rózycska, M. 1999, ApJ, 524, 179
Dere, K. P., Landi, E., Young, P. R., & Zanna, G. 2001, ApJS, 134, 331
Dubner, G., Giacani, E., Goss, W. M., Green, A., & Nyman, L.-A. 2002, A&A, 387, 1047
Dubner, G. M., Giacani, E. B., Goss, W. M., & Winkler, P. F. 1994, AJ, 108, 207
Dubner, G. M., Velázquez, P. F., Goss, W. M., & Holdaway, M. A. 2000, AJ, 120, 1933
Dwek, E. 1981, ApJ, 246, 430
Giacani, E. B., Dubner, G., Cappa, C., & Testori, J. 1998, A&AS, 133, 61
Giacani, E. B., Dubner, G. M., Green, A. J., Goss, W. M., & Gaensler, B. M. 2000, AJ, 119, 281
Giacani, E. B., Dubner, G. M., Kassim, N. E., Frail, D. A., Goss, W. M., Winkler, P. F., & Williams, B. F. 1997, AJ, 113, 1379
Hnatyk, B., & Petruk, O. 1999, A&A, 344, 295
Innes, D. E. 1985, Ph.D. thesis, Univ. London
Jun, B.-I., & Norman, M. L. 1996, ApJ, 472, 245
Landini, M., & Monsignori Fossi, B. C. 1991, A&AS, 91, 183
Malyshkin, L. 2001, ApJ, 554, 561
Matsui, Y., Long, K. S., & Tuohy, I. R. 1988, ApJ, 329, 838
Mazzotta, P., Mazzitelli, G., Colafrancesco, S., & Vittorio, N. 1998, A&AS, 133, 403
Mereghetti, S., Bignami, G. F., & Caraveo, P. A. 1996, ApJ, 464, 842
Milne, D. K., & Haynes, R. F. 1994, MNRAS, 270, 106
Morrison, R., & McCammon, D. 1983, ApJ, 270, 119
Narayan, R., & Medvedev, M. 2001, ApJ, 562, L129
Ostriker, J., & Silk, J. 1973, ApJ, 184, L113
Petruk, O. 2001, A&A, 371, 267
Raga, A. C., de Gouveia dal Pino, E. M., Noriega-Crespo, A., Mininni, P. D., & Velázquez, P. F. 2002, A&A, 392, 267
Raga, A. C., Navarro-González, R., & Villagrán-Muniz, M. 2000, Rev. Mexicana Astron. Astrofis., 36, 67
Raga, A. C., Sobral, H., Villagrán-Muniz, M., Navarro-González, R., & Masciadri, E. 2001, MNRAS, 324, 206
Rho, J., Petre, R., Schlegel, E. M., & Hester, J. J. 1994, ApJ, 430, 757
Sedov, L. 1959, Similarity and Dimensional Methods in Mechanics (New York: Academic)
Shelton, R. L., Cox, D. P., Maciejewski, W., Smith, R. K., Plewa, T., Pawl, A., & Rózycska, M. 1999, ApJ, 524, 192
Sobral, H., Villagrán-Muniz, M., Navarro-González, R., & Raga, A. C. 2000, App. Phys. Lett., 77, 3158
Spitzer, L. 1962, Physics of Fully Ionized Gases (New York: Interscience)
Van Leer, B., 1982, ICASE Rep. No. 82-30 (Langley: ICASE)
Velázquez, P. F., de la Fuente, E., Rosado, M., & Raga, A. C. 2001b, A&A, 377, 1136
Velázquez, P. F., Sobral, H., Raga, A. C., Villagrán-Muniz, M., & Navarro-González, R. 2001a, Rev. Mexicana Astron. Astrofis., 37, 87
White, R. L., & Long, K. S. 1991, ApJ, 373, 543
Willingale, R., West, R. G., Pye, J. P., & Stewart, G. C. E. 1996, MNRAS, 278, 749
Winkler, P. F., & Long, K. S. 1997, ApJ, 491, 829
Young, P. R., Del Zanna, G., Landi, E., Dere, K. P., Mason, H. E., & Landini, M. 2003, ApJS, 144, 135
Zavlin, V. E., Pavlov, G. C., Sanwal, D. & Trümper, J. 2000, ApJ, 540, L25
Zhekov, S. A. & Myasnilov, A. V. 2000, ApJ, 543, L53